Ionized Gas Extended Over 40 kpc in an Odd Radio Circle Host Galaxy

Alison L. Coil[*1], Serena Perrotta[1], David S. N. Rupke[2], Cassandra Lochhaas[3], Christy A. Tremonti[4],

Aleks Diamond-Stanic[5], Drummond Fielding[6] James Geach[7], Ryan C. Hickox[8], John Moustakas[9],

Gregory H. Rudnick[10], Paul Sell[11], Kelly E. Whalen[8]

[1]*Center for Astrophysics and Space Sciences, University of California, 9500 Gilman Dr., La Jolla, CA 92093, acoil@ucsd.edu*

[2]*Department of Physics, Rhodes College, Memphis, TN 38112*

[3]*Space Telescope Science Institute, 3700 San Martin Dr., Baltimore, MD 21218*

[4]*Department of Astronomy, University of Wisconsin-Madison, Madison, WI 53706*

[5]*Department of Physics and Astronomy, Bates College, Lewison, ME 04240*

[6]*Center for Computational Astrophysics, Flatiron Institute, 162 5th Ave, New York, NY 10010*

[7]*Centre for Astrophysics Research, University of Hertfordshire, Hatfield, Hertfordshire AL10 9AB*

[8]*Department of Physics and Astronomy, Dartmouth College, Hanover, NH 03755*

[9]*Department of Physics and Astronomy, Siena College, Loudonville, NY 12211*

[10]*Department of Physics and Astronomy, University of Kansas, Lawrence, KS 66045*

[11]*Department of Astronomy, University of Florida, Gainesville, FL, 32611*

A new class of extragalactic astronomical sources discovered in 2021, named Odd Radio Circles (ORCs)[1], are large rings of faint, diffuse radio continuum emission spanning ∼1 arcminute on the sky. Galaxies at the centers of several ORCs have photometric redshifts of

$z \sim 0.3 - 0.6$, **implying physical scales of several 100 kiloparsecs in diameter for the radio emission, the origin of which is unknown. Here we report spectroscopic data on an ORC including strong [O II] emission tracing ionized gas in the central galaxy of ORC4 at $z = 0.4512$. The physical extent of the [O II] emission is $\sim$40 kpc in diameter, larger than expected for a typical early-type galaxy[2] but an order of magnitude smaller than the large-scale radio continuum emission. We detect a $\sim$200 km s^{-1} velocity gradient across the [O II] nebula, as well as a high velocity dispersion of $\sim$180 km s^{-1}. The [O II] equivalent width (EW, $\sim$50 Å) is extremely high for a quiescent galaxy. The morphology, kinematics, and strength of the [O II] emission are consistent with the infall of shock ionized gas near the galaxy, following a larger-scale, outward moving shock. Both the extended optical and radio emission, while observed on very different scales, may therefore result from the same dramatic event.**

Three ORCs were first discovered[1] in the Evolutionary Map of the Universe Pilot Survey[3] at a frequency of $\sim$1 GHz using the Australian Square Kilometer Array Pathfinder (ASKAP) telescope[4,5]. The ASKAP array has high angular resolution ($\sim$13″), is sensitive to low surface brightness emission, and the pilot survey covers 270 deg^2 of the sky, such that it is able to detect rare, faint objects not previously detected. A fourth ORC (ORC4) was discovered in archival data taken with the Giant MeterWave Radio Telescope (GMRT)[6] at 325 MHz, while additional ORCs were discovered in later ASKAP[7] and MeerKAT data[8]. ORCs exhibit large, limb-brightened rings of radio continuum emission with lower surface brightness emission in the interior. Follow-up MeerKAT data on ORC1 reveals that the radio emission is most likely aged synchrotron, and polarization data show magnetic field lines that are consistent with an expanding shell[9]. The origin

of the radio emission is unknown, with scenarios proposed including Galactic supernovae remnants, double-lobed radio galaxies, ring galaxies, and gravitationally-lensed Einstein rings[1]. However, the most likely scenarios involve a shock from an outflowing galactic wind or a blast wave driven by merging supermassive black holes[7].

To search for an optical counterpart to ORCs, we observed ORC4 with the Keck Cosmic Web Imager (KCWI[10]) and detected strong [O II] and weak Mg II and [Ne III] line emission in a spatially-integrated spectrum (Extended Data Fig. 1). The [O II] luminosity is $7.1 \times 10^{41}\ erg\ s^{-1}$, near the break of the [O II] luminosity function at $z \sim 0.5$[11]. The restframe [O II] EW is 50 Å in the spatially-integrated spectrum, which is an order of magnitude higher than what is typically found in red, early-type galaxies[12]. Long-slit optical spectroscopy of ORC4 that includes wavelengths redward of the KCWI data reveals low-ionization nuclear emission-line region (LINER)-like line ratios (D. S. N. Rupke et al., manuscript in preparation).

A spectral energy distribution (SED) fit to the optical and infrared emission in the central galaxy of ORC4 (Extended Data Fig. 2) reveals that the galaxy is massive ($\log M_*/M_\odot = 11.27 \pm 0.06$) and has an old stellar population, with a stellar age of $t_{age} = 6.0\ (+/-1.6)$ Gyr. While the SED fit has only a 3% contribution from an AGN, the radio continuum emission in this galaxy[1] is likely due to an AGN, as there is no indication of on-going star formation. The observed radio flux of 1.43 mJy at 325 MHz corresponds to a luminosity of $1.24 \times 10^{24}\ W\ Hz^{-1}$ at a restframe frequency of 200 MHz, given the redshift and radio spectral index[1]; this is 1.5 orders of magnitude fainter than the break in the radio AGN luminosity function[13].

The [O II] emission is bright enough to create spatially-resolved maps to probe the morphology, extent, and resolved kinematics of the ionized gas. Fig. 1 shows a map of the [O II] surface brightness, the peak of which is $2.3 \times 10^{-16} \ erg \ s^{-1} \ cm^{-2} \ arcsec^{-2}$. The azimuthally-averaged surface brightness profile (Fig. 2) reveals a strong central concentration of the [O II] emission, in contrast to the larger-scale limb-brightened radio emission. The radial extent is $\sim$20 kpc ($\sim$40 kpc in diameter), and the half light (or "effective") radius is 3.4 kpc, deconvolved with the seeing. The [O II] radial extent is an order of magnitude smaller than the radio continuum emission in ORC4, which extends $\sim$200 kpc in radius.

The [O II] restframe EW spatial map (Fig. 1, panel d) does not show strong asymmetry. The restframe EW at the center of the nebula is >70 Å(Fig. 2), and at a radius of 15 kpc (shown here at $R/R_e = 3$, relative to the galaxy half-light radius) it is $\sim$25 Å. For comparison, [O II] EW profiles are shown for massive, nearby early-type galaxies, where integral field data reveals that 38% of galaxies with $> 10^{11.5}$ $M_\odot$ have [O II] emission[2]. The median [O II] EW of these comparison galaxies is 4.8 Å, and the maximum EW is 28 Ang. The [O II] EW in ORC4 is therefore an order of magnitude higher than is typically seen in massive, early-type galaxies. The maximal radial extent of the [O II] in these comparison galaxies varies from 0.6-18.2 kpc, with a median maximal extent of 2.3 kpc. The [O II] emission in ORC4, detected to a radius of $\sim$20 kpc, is therefore unusually spatially extended. It is extended not only in the sense that it is not from the nucleus of the galaxy, but the maximal extent is an order of magnitude higher than in comparable galaxies.

The kinematics of the [O II] emission (Fig. 3) reveal an asymmetric velocity gradient across

the nebula, from $+170 \text{ km s}^{-1}$ at the northern edge to -50 km s^{-1} at the southern edge. A north-south position-velocity diagram (Fig. 3, panel c) highlights the asymmetry in the velocity gradient. The velocity dispersion varies from a minimum of $\sim 60 \text{ km s}^{-1}$ at the edges of the nebula to ~ 180 km s^{-1} in the center and up to $\sim 250 \text{ km s}^{-1}$ at the northern and western edges.

There are multiple possibilities for the origin of the extended [O II] emission observed in ORC4. Given the properties of the ionized gas and host galaxy, it is unlikely that it is associated with the interstellar medium (ISM) of the galaxy or an AGN or AGN-driven outflow or due to a cooling flow (see Methods section "Alternative scenarios for ionized gas origin" for details.) Another possibility is that it is associated with the same energetic event that created the large-scale radio emission which identified the source as an ORC. The LINER-like line ratios of ORC4 point to the ionized gas arising from shocks[14]. One of the possible scenarios for the creation of ORCs is a shock from a starburst wind, which would create multiple shocks on different scales including both a forward moving shock on large scales and a reverse shock, sometimes called a wind shock, on smaller scales, with a contact discontinuity in between[15, 16]. In a model of galactic winds created by starburst activity[17], the forward shock can exist on scales of >100 kpc, while the reverse shock exists on scales of ~ 10-50 kpc. Once the starburst episode that initially drove the outflow has shut off, the gas heated by the reverse shock can then travel backwards towards the central galaxy[18], moving to smaller scales. The shocked wind expands to fill the under-pressurized inner region that has been cleared by the outward-moving forward shock and may produce a turbulent, energetic medium full of additional shocks by interacting with gas in and around the galaxy. Wind re-heated in this way by the reverse shock may then radiatively cool giving rise to ionized gas emission on

the scale of the galaxy. Meanwhile the forward shock, which has continued to propogate outwards, creates synchrotron emission on large scales. This scenario differs than that proposed by Norris et al. (2022), where the large-scale radio emission is associated with the reverse shock; we propose that is associated with the forward shock. In theoretical models the large-scale forward shock can propogate to scales of hundreds of kiloparsecs on timescales of several Gyr[18]. Recent cosmological simulations focusing on galaxy mergers as the cause of ORCs[19] show that additional shocks are seen on smaller scales as well.

This scenario is consistent with observations of ORC4 in multiple ways. The best fit SED model indicates that the galaxy had a burst of star formation ∼1 Gyr ago and is no longer forming stars. The scale, morphology, and surface brightness distribution of the [O II] emission are consistent with expectations for the shocked wind gas falling back towards the galaxy, which could also lead to an asymmetric velocity gradient and high velocity dispersion due to turbulence. The strength of the [O II] emission is also consistent with being due to shocks, which are known to lead to an enhancement of [O II][20], and/or may reflect mixing between hot and cool gas phases, which can lead to additional gas cooling[21,22].

To further test a starburst-driven wind model for ORCs, we ran a suite of simulations that launch a wind from an isolated galaxy and followed the evolution of the forward and reverse shocks (Fig. 4). Our goal was to reproduce the forward shock radius (∼200 kpc) and Mach number (∼1-2) required to produce the observed synchrotron emission, the scale of the reverse shock and subsequent infalling shocked wind (∼20 kpc), the elevated velocity dispersion of the shocked wind

gas ($\sim$150 km s^{-1}), and the age of the wind bubble ($\sim$1 Gyr). We found that these parameters could be reproduced with a wind that is launched with a velocity of 450 km s^{-1} and a mass outflow rate of 200 $M_\odot$yr^{-1}, which blows for 200 Myr. (See Methods section "Outflowing galactic wind simulation" for details.) The high mass outflow rate needed is potentially consistent with the SED fit results for the central galaxy in ORC4, which require a high fraction of the total stellar mass (61%) produced in a starburst which presumably had a high SFR, which could have created an outflow with a high mass outflow rate. The features of the wind model presented here are generic features of an energy and mass injection, without regard to the source of the injection. In order for the wind bubble to survive at a Mach number of $\sim$1-2 to a scale of $\sim$200 kpc, the density of the CGM must be lower than is typically assumed for a galaxy of stellar mass 10^{11} $M_\odot$, though the density is still feasible (simulations find the CGM density of a Milky Way-mass halo spans six orders of magnitude[23]). As ORCs appear to be a rare phenomena, they may arise only in situations where the galaxy progenitor and CGM parameters are favorable. This simulation shows that a single event such as a strong starburst can launch a wind that simultaneously produces both the large-scale radio emission and the smaller-scale [O II] emission scale, when observed $\sim$1 Gyr after the event.

We have been studying outflowing galactic winds in massive ($\sim 10^{11}$ M$_\odot$) starburst galaxies at $0.4 < z < 0.8$[24]; most are late-stage major mergers[25]. These starburst galaxies are driving extremely fast multi-phase gas outflows with velocities of $\sim$2000 km s^{-1} and mass outflow rates of $\gtrsim$200 $M_\odot$yr^{-1}[26,27]. Their space densities ($1 \times 10^{-6} Mpc^{-3}$) are similar to that of post-starburst galaxies and ultra-luminous infrared galaxies (ULIRGs)[28]. KCWI data reveals [O II] nebulae in these galaxies of sizes 30-100 kpc[29] (S. Perrotta et al., in preparation).

7

Though their space density is potentially lower (estimated at $\sim 2 \times 10^{-8} Mpc^{-3}$)[9], ORCs may be a later stage of a similar phenomenon. In order for ORCs to be the result of a starburst wind shock the starburst must have been extreme[9], with a high mass outflow rate, and the density of the CGM must be low. The massive starburst galaxies we have been studying at $z \sim 0.5$ have such extreme outflow properties[30]. In the model of an ancient, starburst-driven wind, the ancestors of ORCs must resemble these compact starbursts in some way. These ORC wind relics may then be a direct tracer of powerful outflows from earlier energetic starburst events.

1. Norris, R. P. *et al.* Unexpected circular radio objects at high Galactic latitude. PASA **38**, e003 (2021).

2. Pandya, V. *et al.* The MASSIVE Survey. VI. The Spatial Distribution and Kinematics of Warm Ionized Gas in the Most Massive Local Early-type Galaxies. *Astrophys. J.* **837**, 40 (2017).

3. Norris, R. P. *et al.* The Evolutionary Map of the Universe pilot survey. PASA **38**, e046 (2021).

4. Johnston, S. *et al.* Science with the Australian Square Kilometre Array Pathfinder. PASA **24**, 174 (2007).

5. McConnell, D. *et al.* The Australian Square Kilometre Array Pathfinder: Performance of the Boolardy Engineering Test Array. PASA **33**, e042 (2016).

6. Ananthakrishnan, S. The Giant Meterwave Radio Telescope / GMRT. *Journal of Astrophysics and Astronomy Supplement* **16**, 427 (1995).

7. Koribalski, B. S. *et al.* Discovery of a new extragalactic circular radio source with ASKAP: ORC J0102-2450. *Mon. Not. Royal Astron. Soc.* **505**, L11–L15 (2021).

8. Koribalski, B. S. *et al.* MeerKAT discovery of a double radio relic and odd radio circle. *arXiv e-prints* arXiv:2304.11784 (2023). `2304.11784`.

9. Norris, R. P. *et al.* MeerKAT uncovers the physics of an odd radio circle. *Mon. Not. Royal Astron. Soc.* **513**, 1300–1316 (2022).

10. Morrissey, P. *et al.* The Keck Cosmic Web Imager Integral Field Spectrograph. *Astrophys. J.* **864**, 93 (2018).

11. Zhu, G., Moustakas, J. & Blanton, M. R. The [O II] λ3727 Luminosity Function at z ~1. *Astrophys. J.* **701**, 86–93 (2009).

12. Yan, R. *et al.* On the Origin of [O II] Emission in Red-Sequence and Poststarburst Galaxies. *Astrophys. J.* **648**, 281–298 (2006).

13. Franzen, T. M. O. *et al.* The GLEAM 200-MHz local radio luminosity function for AGN and star-forming galaxies. PASA **38**, e041 (2021).

14. Yan, R. & Blanton, M. R. The Nature of LINER-like Emission in Red Galaxies. *Astrophys. J.* **747**, 61 (2012).

15. Faucher-Giguère, C.-A. & Quataert, E. The physics of galactic winds driven by active galactic nuclei. *Mon. Not. Royal Astron. Soc.* **425**, 605–622 (2012).

16. King, A. & Pounds, K. Powerful Outflows and Feedback from Active Galactic Nuclei. *Ann. Rev. of Astron. Astrophys.* **53**, 115–154 (2015).

17. Thompson, T. A., Quataert, E., Zhang, D. & Weinberg, D. H. An origin for multiphase gas in galactic winds and haloes. *Mon. Not. Royal Astron. Soc.* **455**, 1830–1844 (2016).

18. Lochhaas, C., Thompson, T. A., Quataert, E. & Weinberg, D. H. Fast winds drive slow shells: a model for the circumgalactic medium as galactic wind-driven bubbles. *Mon. Not. Royal Astron. Soc.* **481**, 1873–1896 (2018).

19. Dolag, K., Böss, L. M., Koribalski, B. S., Steinwandel, U. P. & Valentini, M. Insights on the Origin of Odd Radio Circles from Cosmological Simulations. *Astrophys. J.* **945**, 74 (2023).

20. Allen, M. G., Groves, B. A., Dopita, M. A., Sutherland, R. S. & Kewley, L. J. The MAPPINGS III Library of Fast Radiative Shock Models. *Astrophys. J. Suppl.* **178**, 20–55 (2008).

21. Gronke, M. & Oh, S. P. How cold gas continuously entrains mass and momentum from a hot wind. *Mon. Not. Royal Astron. Soc.* **492**, 1970–1990 (2020).

22. Fielding, D. B. & Bryan, G. L. The Structure of Multiphase Galactic Winds. *Astrophys. J.* **924**, 82 (2022).

23. Simons, R. C. *et al.* Figuring Out Gas & Galaxies in Enzo (FOGGIE). IV. The Stochasticity of Ram Pressure Stripping in Galactic Halos. *Astrophys. J.* **905**, 167 (2020). `2004.14394`.

24. Tremonti, C. A., Moustakas, J. & Diamond-Stanic, A. M. The Discovery of 1000 km s^{-1} Outflows in Massive Poststarburst Galaxies at z=0.6. *Astrophys. J.* **663**, L77–L80 (2007).

25. Sell, P. H. *et al.* Massive compact galaxies with high-velocity outflows: morphological analysis and constraints on AGN activity. *Mon. Not. Royal Astron. Soc.* **441**, 3417–3443 (2014).

26. Rupke, D. S. N. *et al.* The Ionization and Dynamics of the Makani Galactic Wind. *Astrophys. J.* **947**, 33 (2023).

27. Perrotta, S. *et al.* Kinematics, Structure, and Mass Outflow Rates of Extreme Starburst Galactic Outflows. *Astrophys. J.* **949**, 9 (2023). `2303.07448`.

28. Whalen, K. E. *et al.* The Space Density of Intermediate-redshift, Extremely Compact, Massive Starburst Galaxies. *Astron. J.* **164**, 222 (2022).

29. Rupke, D. S. N. *et al.* A 100-kiloparsec wind feeding the circumgalactic medium of a massive compact galaxy. *Nature* **574**, 643–646 (2019).

30. Diamond-Stanic, A. M. *et al.* Compact Starburst Galaxies with Fast Outflows: Central Escape Velocities and Stellar Mass Surface Densities from Multiband Hubble Space Telescope Imaging. *Astrophys. J.* **912**, 11 (2021).

31. Dey, A. *et al.* Overview of the DESI Legacy Imaging Surveys. *Astron. J.* **157**, 168 (2019).
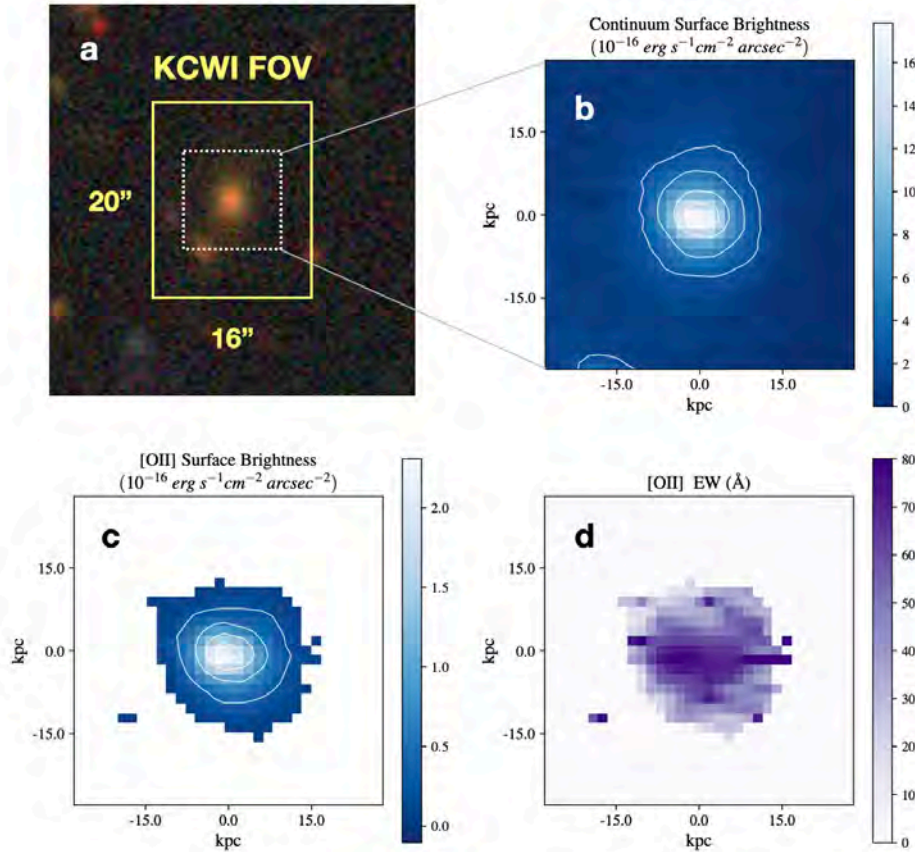
Figure 1 **Optical stellar continuum and [O II] emission in ORC4.** (a) DESI Legacy Survey DR9[31]

optical grz image of ORC4, spanning $40''$ on each side. The KCWI field of view (FOV) is shown

with a yellow box, and the dotted white box traces the central $10'' \times 10''$, shown in the remaining

panels. (b) Stellar continuum surface brightness image from KCWI, integrated over the observed

wavelength range 4200-5300 Å, with axes labeled in kpc from the center of the galaxy. White

contours show levels of 2.5, 5, 10, and $15 \times 10^{-16}\ erg\ s^{-1}\ cm^{-2}\ arcsec^{-2}$. (c) [O II] surface

brightness image, showing spaxels with S/N$\geq$3. White contours show surface brightness levels

of 0.3, 0.8, 1.4, and $1.9 \times 10^{-16}\ erg\ s^{-1}\ cm^{-2}\ arcsec^{-2}$. (d) [O II] restframe equivalent width (EW)

map.

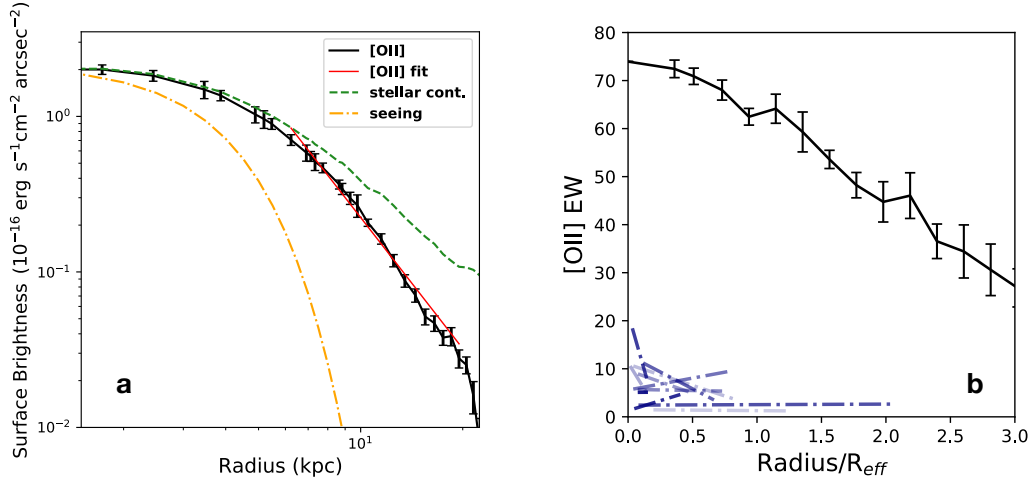**Figure 2** **Radial surface brightness and equivalength width profile of the [O II] emission.** (a) The

black line shows the [O II] radial surface brightness profile, with 1σ errors; the nebula has a radial

extent of ∼20 kpc. The green line shows the radial profile of the stellar continuum, normalized to

the peak of the [O II] profile, and the orange line shows the extent of the ground-based seeing,

also normalized to the [O II]. The red line is the best fit slope to the [O II] radial profile (beyond 5

kpc, outside the seeing disk) of -2.8. (b) The black line shows the restframe equivalent width (EW)

profile of the [O II] emission in ORC4 as a function of radius from the center of the galaxy, relative

to the stellar half light radius ($R_e = 4.8$ kpc), with 1σ errors. For comparison, purple dot-dashed

lines show the [O II] EW radial profile fits for nearby massive, early-type galaxies[2].

13

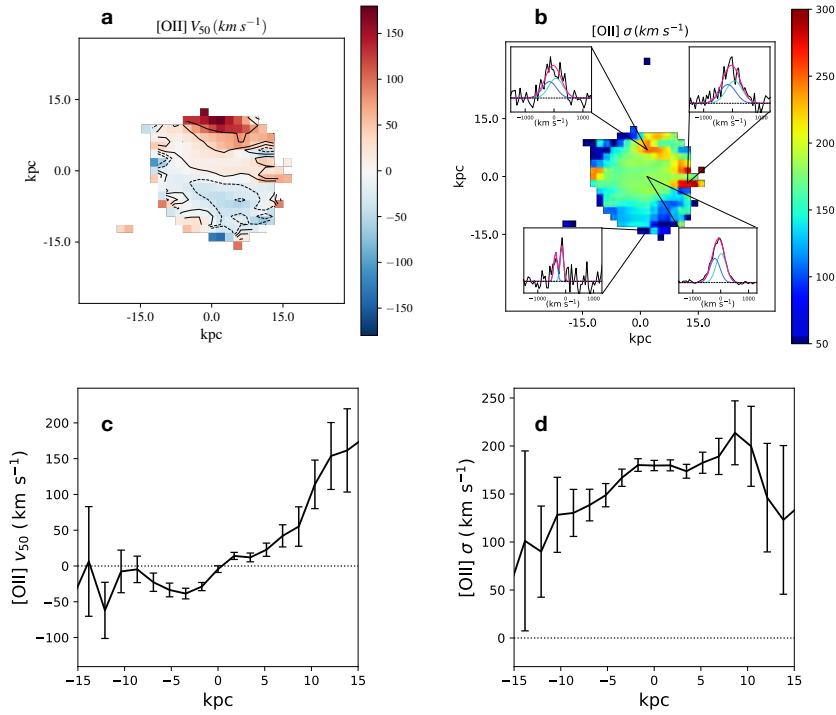**Figure 3** **Kinematics of the [O II] emission.** (a) Velocity map of the [O II] emission showing the

central velocity (V_{50}) of the ionized gas relative to the systemic redshift of the source, $z = 0.4512$.

Contours mark where the central velocity is -50, -25, 0, 25, 75 km s^{-1}. A clear velocity gradient is

seen from north to south across the nebula. (b) The velocity dispersion σ of the [O II] emission,

showing a higher dispersion in the center, north, and west regions of the nebula. Insets show spectra

at various locations around the nebula, highlighting areas with high and low velocity dispersion.

Blue and cyan lines in the insets show Gaussian fits to the individual [O II] emission lines. (c) A

position-velocity diagram through the center of the [O II] nebula along the north-south direction,

averaging across the central 5 columns, with 1σ errors. (d) The velocity dispersion through the

14

center of the nebula along the north-south direction, averaging across the central 5 columns, with
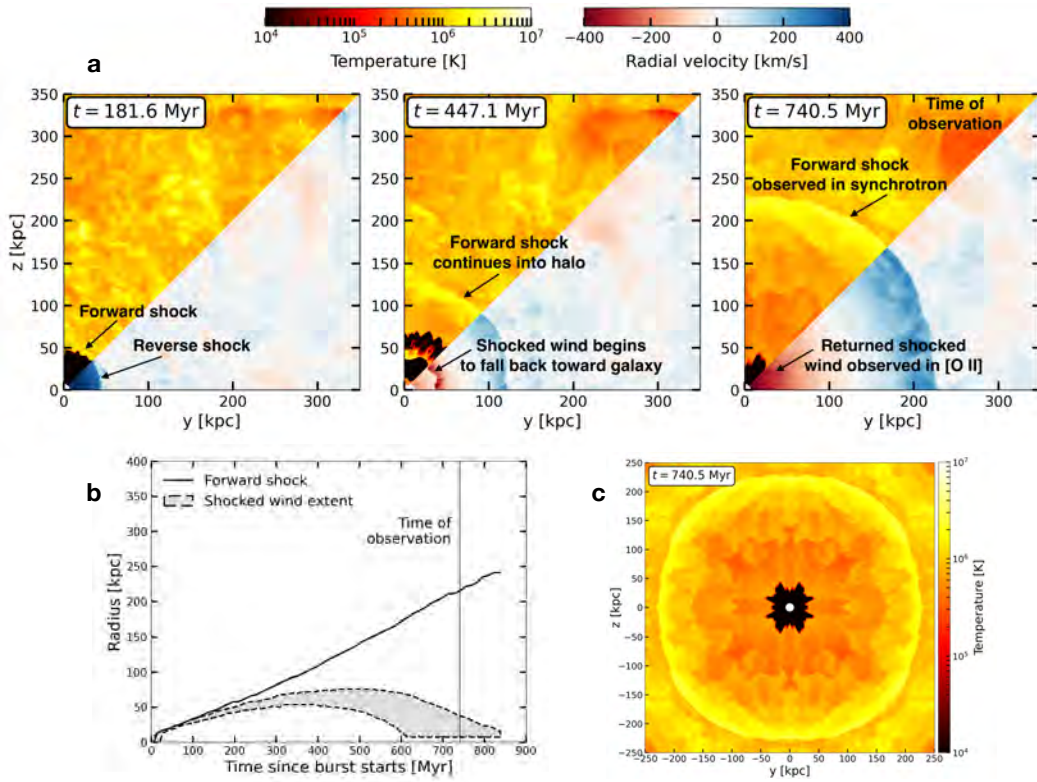
1σ errors.

Figure 4 **Simulation of starburst-driven wind.** (a) Two-dimensional maps of gas temperature

(upper left half of each panel) and gas radial velocity relative to the galaxy (lower right half of each

panel), shown such that red colors indicate material falling onto the galaxy and blue colors indicate

material outflowing from the galaxy, at three times since the onset of the starburst. The wind blows

for 200 Myr, after which wind material that has been heated by the reverse shock falls back towards

the galaxy, while the forward shock continues to expand into the halo. (b) Radius of the large-scale

forward shock and the smaller-scale inner and outer boundaries of the shocked wind as a function

15

of time since the onset of the starburst. (c) Spherical two-dimensional map (mirrored from the one quadrant simulated) of the gas temperature at the time of observation, 740 Myr after the onset of the starburst and 540 Myr since the star formation and wind ceased. The large yellow ring corresponds to where radio synchrotron emission is expected to arise, while the smaller-scale black region surrounding the central galaxy contains cool gas that could be observed as [O II] emission.

Methods

KCWI observations and data reduction. We observed ORC4 (RA=15:55:24.63 Dec=+27:26:34.3) with KCWI on the Keck II telescope on March 27, 2022. The weather was clear and the seeing was ∼0.9″; we observed at a position angle of 0 degrees and an airmass of 1.2. We used the blue low dispersion (BL) grating and the medium slicer on KCWI, which provides a spectral resolution of R=1800, a spaxel size of $0.29″ \times 0.69″$, and a FOV of $16″ \times 20″$ per pointing. We configured the instrument to a central wavelength of 4700 Å and used a detector binning of 2×2, which provides wavelength coverage of $3700 - 5700$ Å. We observed a total of three KCWI pointings, each spanning $16″ \times 20″$, integrating for 20 minutes per pointing. One pointing was centered on ORC4; these are the data we report here. Two additional pointings were centered 18″ to the north and to the south of the first pointing; no emission was detected at either offset pointing. In total we observed a field of view of $16″ \times 56″$.

We reduced the data using the IDL version of the KCWI Data Extraction and Reduction Pipeline (v1.2.1) and the IFSRED IDL library [1]. Sky subtraction was performed using the IDL pipeline with manual selection of a sky mask region within each pointing. The standard star BD+33d2642 was used for flux calibration. Following the pipeline stages, we resampled the data onto $0.29″ \times 0.29″$ spaxel grids using the routine IFSR_KCWIRESAMPLE. The resulting data cube has dimensions of 56×66 spaxels, covering $16.2″ \times 19.1″$. Assuming a ΛCDM Planck 2020 cosmology[2] the physical dimensions of a single KCWI pointing correspond to 97 kpc $\times$ 114 kpc at z=0.4512.

Spatially-integrated spectrum and line fluxes. In addition to having spectra at each spaxel in the full datacube, we created three spatially-integrated spectra by summing the observed flux in rectangular apertures spanning the central 3×3, 7×7, and 15×15 spaxels, corresponding to physical scales of 5, 12, and 26 kpc, respectively. We detect strong [O II] 3726Å and 3729Å and weak Mg II 2796Å and 2803Å and [Ne III] 3869Å line emission in the spatially-integrated spectra (Extended Data Fig. 1), which also include continuum emission from stars in the central galaxy. The [O II] doublet is blended in most spaxels, due to high velocity dispersion. The [O II] and [Ne III] emission trace ionized gas; while Mg II is ionized gas, it is a resonant transition to the ground state and has an ionization state that overlaps with neutral hydrogen, such that it traces neutral gas[3]. Both [O II] and Mg II trace gas temperatures of $\sim 10^4$ K. The [O II] doublet is observed at air wavelengths of 5407.2 and 5411.2Å; the spectroscopic redshift of ORC4 is therefore $z = 0.4512$. The [Ne V] 3426Å emission line is not detected.

The spatially-integrated spectrum spanning the largest scales is used to determine integrated fluxes. The flux of the [O II] doublet, corrected for Galactic extinction, is $8.8\ (\pm0.1) \times 10^{-16}\ erg\ s^{-1}\ cm^{-2}$. The total Mg II flux is $0.64\ (\pm0.13) \times 10^{-16}\ erg\ s^{-1}\ cm^{-2}$; the ratio of the [O II] to Mg II flux is 14. The restframe EW of the Mg II emission is 7 Å, and the observed ratio of the blue to red Mg II emission doublet is 1.9, close to the intrinsic flux ratio of 2.0, which implies that the gas is optically thin[3] and not substantially impacted by absorption. The flux of the [Ne III] 3869 Å line is $0.72\ (\pm0.11) \times 10^{-16}\ erg\ s^{-1}\ cm^{-2}$. The Mg II and [Ne III] emission are too weak to detect in spatially resolved maps. In the spatially-integrated spectrum the kinematics of the Mg II and [Ne III] emission are consistent with the [O II] emission, both in terms of velocity centroid and

width.

Spectral cube analysis. We fit Gaussian profiles to the observed emission lines, fitting Mg II, [O II], and [Ne III] in the spatially-integrated spectra and [O II] in each spaxel of the full datacube. As the [O II] doublet is blended, we fix the [O II] flux ratio to be 1.2, corresponding to an electron density of $\sim 200 \; cm^{-3}$. We did not tie the kinematics of the Mg II, [O II], and [Ne III] lines together. The continuum level around each line is determined locally using the flux within 40 Å on either side of the emission singlet or doublet.

We define V_{50} as the central velocity of the emission, as determined by the centroid of the Gaussian fit. The velocity dispersion σ is also determined by the Gaussian fit, from which the instrumental resolution is subtracted in quadrature. The ratio of V_{50} to σ in ORC4 is low, with a median value of 0.19; this is an order of magnitude lower than what is seen in star-forming galaxies[4]. The statistical errors on σ range from $\sim$10 km s^{-1} at the center of the nebula to $\sim$20 km s^{-1} at a radius of 5 kpc and $\sim$65 km s^{-1} at a radius of 10 kpc. The systematic errors on σ are subdominant; changing the [O II] flux ratio from extreme values of 1.0 to 1.5 results in median differences to σ of only $\sim$2 km s^{-1} and does not change our results.

The systemic redshift of $z = 0.4512$ is defined by the centroid of the observed wavelengths of the [O II] emission in the largest spatially-integrated spectrum. The [O II] EW is calculated by comparing the total flux in the [O II] doublet to the fit of the continuum level around [O II], which is divided by $(1 + z)$ to obtain a restframe EW.

In Figs. 1 and 3 we show those spaxels for which the [O II] flux has a signal to noise ratio

of 3 or greater. We calculate the surface brightness radial profile using RADP in IDL and fit for the slope of the [O II] profile from $6 - 15$ kpc, beyond the region of the seeing disk. The errors shown in Fig. 2 are standard errors, calculated from the variation in the surface brightness within that radial bin, and the errors in Fig. 3 are the standard errors calculated from the variation in the central velocity fit across the central five spaxels of the nebula.

Surface brightness profile and Sersic fit. The central $\sim$5 kpc of the radial surface brightness profiles are not resolved due to the observational seeing; from 6-15 kpc the best fit power law slope to the [O II] profile is -2.8. We fit the radial surface brightness profile of both the [O II] nebula and the stellar continuum with a Sersic profile, convolving with the PSF of the observations. The Sersic profile is:

$$I(r) = I_e \, exp\{-(1.9992n - 0.3271) \, [(r/r_e)^{(1/n)} - 1)]\} \tag{1}$$

where I is the surface brightness as a function of radius, I_e is the surface brightess at the half light radius, r_e, and n is the Sersic index, which reflects the amount of curvature in the profile. We use CONVOL in IDL to convolve this profile with a Gaussian with a FWHM of $0.9''$ to account for the seeing. The PSF-corrected best-fit Sersic index to the [O II] emission yields $n = 1$, while for the stellar continuum the best fit is $n = 2$. We verified these results using GALFIT with a Gaussian PSF. The stellar emission in the ORC4 central galaxy is more extended than the [O II] emission; the galaxy half light radius is 4.8 kpc.

Stellar mass and age estimation. There is another galaxy near ORC4, as seen in Fig. 1. Long-slit spectroscopy reveals that it is at the same redshift as ORC4 (D. S. N. Rupke et al., in preparation) and is 36 kpc away; these galaxies are near enough to likely be interacting[5]. We estimate stellar

masses and ages for ORC4 and its companion galaxy by fitting the spectral energy distributions (SEDs) using PROSPECTOR [6], using a redshift of $z = 0.4512$ for both galaxies (Extended Data Fig. 2). PROSPECTOR utilizes gridless Bayesian parameter estimation and incorporates Markov chain Monte Carlo (MCMC) posterior sampling with EMCEE to infer the properties of the underlying stellar populations using Flexible Stellar Population Synthesis models (FSPS)[7]. For ORC4, we fit broadband SDSS DR8[8] *ugriz* and *WISE*[9] W1 and W2 photometry, and for the companion galaxy we fit SDSS *ugriz* photometry. We assume a Kroupa initial mass function[10] and a power law attenuation curve with index = -0.7.

For ORC4 we assume a parametric τ-model star formation history with a burst where the star formation rate is given as $SFR \sim \exp(t_{age}/\tau)$, and we allow an AGN contribution. The free parameters in the model are the galaxy stellar mass and age (t_{age}), the fraction of stellar mass formed in the burst (f_{burst}), the fraction of the stellar age at which a starburst occurred ($f_{age,burst}$), τ, and the fraction of the light that is due to an AGN. All timescales have units of Gyr. We set a log-normal prior on the stellar mass with a mode of $\ln(M_*/M_\odot) = 23$ and $\sigma = 15$, as well as a log-uniform prior on t_{age} such that $0.1 < t_{age}/\text{Gyr} < t_{universe}(z)$ where $t_{universe}(z)$ is the age of the universe at the given redshift of $z = 0.4512$. For the companion galaxy we similarly assume a parametric τ-model star formation history, but we do not include a burst or an AGN contribution. Stellar mass and t_{age} are the only free parameters in the model for the companion galaxy, and we assume the same priors that we implemented for ORC4. For both ORC4 and its companion galaxy the stellar metallicity ($\log Z_*/Z_\odot$) is updated for each random draw of M_* within ± 0.1 dex of the stellar mass-metallicity relation[11].

The SED fit to the companion galaxy reveals that it is massive, with $\log\,(M_*/M_\odot) = 10.60\,(+0.10/-0.16)$, and old, with $t_{age} = 7.0\,(+1.2/-1.4)$ Gyr, similar to what is found for the ORC4 central galaxy.

Radio luminosity conversion. To convert the observed radio flux of the central source in ORC4 to a luminosity at a restframe of 200 MHz, we use the following equation:

$$L_\nu = 4\pi D_L^2 (1+z)^{-(1+\alpha)} (\nu/\nu_{obs})^{(1+\alpha)} (\nu_{obs}/\nu) F_{\nu_{obs}} \tag{2}$$

where D_L is the luminosity distance, α is the observed spectral index of ORC4 of -0.92, ν is the observed-frame frequency of the radio luminosity we are deriving, here equal to 200 MHz $\times (1+z)$, ν_{obs} is the observed frequency of 325 MHz, and $F_{\nu_{obs}}$ is the observed flux of 1.43mJy. We use this same equation to convert to a restframe 1.4 GHz luminosity.

Ionized gas mass estimate. We use the [O II] luminosity to estimate the mass of the warm ionized gas in ORC4. Following Pandya et al. (2017)[2], we assume [O II]/H$\beta = 6$ to compute an Hβ luminosity and then use the following equation:

$$M_{H\beta} = 28.2 \times 10^8 L_{H\beta,43}\, n_{e,100}^{-1}\, M_\odot \tag{3}$$

where $L_{H\beta,43}$ is the Hβ luminosity in units of $10^{43}\,erg\,s^{-1}$ and $n_{e,100}$ is the electron density in units of 100 cm^{-3}. We assume $n_{e,100}=1$ to facilitate a comparison with the results of Pandya et al. (2017). The ratio of [O II]/Hβ assumed is similar to the value found in long-slit spectroscopy of ORC4 ($\sim$5.5, D. S. N. Rupke et al., in preparation).

Alternative scenarios for ionized gas origin. There are several alternative scenarios for the origin of the ionized gas in ORC4. The first is that it is associated with the interstellar medium (ISM) of

the central galaxy. The velocity gradient in the ionized gas could be due to rotation of the galaxy; many early-type galaxies have spatially extended, rotating [O II] emission[2]. However, the velocity gradient is asymmetric and the radial extent and the velocity dispersion of the [O II] emission in ORC4 are unusually high. From the [O II] luminosity we estimate a warm ionized gas mass of $3 \times 10^7 \ M_\odot$, which is over an order of magnitude higher than that found for massive early-type galaxies[2]. Additionally, the observed [O II] EW is far higher than what is seen in similar early-type galaxies, such that it is very unlikely that this ionized gas in ORC4 is simply cool gas in the ISM of the central galaxy.

Another possibility is that ORC4 may have a bipolar outflowing wind driven by the central AGN, creating the extended [O II] emission. "Red geysers" are early-type galaxies that have bisymmetric EW maps with strong emission lines that appear to trace large-scale outflows[12,13]. Red geysers account for 5-10% of local, early-type galaxies[14]. AGN-driven outflows can result in ionized gas velocity gradients, and the central galaxy in ORC4 does have an AGN, such that it is plausible that it has an AGN-driven outflow. However, such outflows are typically not circular and radio AGN outflows in particular are jet driven and collimated[15]. Additionally, the [O II] EW map of ORC4 does not display the collimated, bisymmetric observational signatures of red geyser EW maps. Finally, the [O II] luminosity of ORC4 is two magnitudes higher than what is expected for a typical AGN with the same radio continuum luminosity (Extended Data Fig. 3), and the SED fit to the optical and infrared emission finds that only 3% of the light is from an AGN component. Thus another mechanism is required to explain the strong, extended [O II] emission, and the high luminosity and EW in particular, in ORC4.

It is also unlikely that the [O II] emission could result from a cooling flow as ionized gas in cooling flows typically has a complex, and often filamentary, morphology[16]. Additionally, in order for a cooling flow to be sustained the circumgalactic medium should be well settled and not have any disrupting events; the presence of the large-scale radio emission argues against this. This galaxy also does not appear to be in a well-defined overdensity or galaxy cluster [5] where cooling flows might be expected.

Outflowing galactic wind simulation. We run the spherically-symmetric wind simulation using the Athena hydrodynamics code. The galaxy is modeled as an isolated, spherical wind injection region of radius $r = 7$ kpc. The gravitational potential is provided by a static NFW halo of virial mass 10^{13} $M_\odot$, which was chosen from the low-redshift stellar mass to halo mass abundance matching relation [17] for a galaxy of stellar mass $\sim 10^{11.2}$ $M_\odot$, similar to the value estimated for ORC4's central galaxy. The simulated circumgalactic medium is initialized to be in isothermal hydrostatic equilibrium with $T = 10^6$ K, close to the virial temperature for a halo of mass 10^{13} $M_\odot$, and with a gas density near the wind injection region of 10^{-26} g cm^{-3}. The circumgalactic medium is initialized with random velocity and density perturbations with amplitudes on the order of 0.2 times the virial velocity and 0.3 times the density, respectively. The wind turns on immediately at the beginning of the simulation and blows spherically-symmetrically with a velocity of 450 km s^{-1} and with a mass outflow rate of 200 $M_\odot$yr^{-1}, and then the wind turns off at t = 200 Myr. We run just one octant of the sphere to reduce computational costs. The simulation domain is a cube with side length 350 kpc where the wind injection region is located in one corner, at the origin. There are three levels of static mesh refinement: within a 44 kpc cube cornered at the origin, and thus closest

to the wind injection region, the spatial resolution is 438 pc. The resolution decreases to 877 pc out to the edges of a 175 kpc cube, and then again to 1.75 kpc out to the edge of the simulation domain at 350 kpc.

In the simulation that most closely matches the observational inputs, at 740 Myr after the starburst begins, or 540 Myr since the star formation and resulting wind have ceased (as the wind blows for 200 Myr), the forward shock is located at 215 kpc in radius and has a Mach number of 1.3, consistent with the shock Mach number required to produce the observed synchrotron emission in ORCs[19]. At this same time, the previously-shocked wind that gives rise to the [O II] emission is falling back toward the galaxy and extends from a radius of 0 to 35 kpc. The velocity dispersion of the previously-shocked wind gas that is returning to the galaxy is $\sim$120 km s^{-1} within a 20 kpc radius, somewhat lower than the [O II] velocity dispersion observed in ORC4. The velocity dispersion in this simulation is a lower limit on the expected velocity dispersion of [O II] emitting gas, as the simulation is not resolving the chaotic series of shocks that are likely producing the [O II] emission within the simulated 10^4 K shocked wind region. The parameters of the wind (velocity, mass outflow rate, the timescale that the wind is "on") and the halo (virial mass, temperature, density) were chosen to produce results that match the properties of ORC4, though we found that a wide range of parameters were generically able to produce a forward shock on large scales and shocked wind falling back to the galaxy on small scales that could be observed hundreds of Myr after the wind from the galaxy had ceased. The simulation does not predict observed [O II] emission line luminosities or the ionized gas mass in the shocked wind gas due to the computational difficulty of radiative transfer modeling.

Data and Code Availability. Raw data generated at the Keck Observatory are available at the Keck Observatory Archive (koa.ipac.caltech.edu) following the standard 18-month proprietary period after the date of observation. The reduced KCWI spectral datacube and the results of the [O II] emission line fits are available on Zenodo at https://doi.org/10.5281/zenodo.8377942. The code used is available upon request from the first author.

1. Rupke, D. S. N. IFSRED: Data Reduction for Integral Field Spectrographs. Astrophysics Source Code Library, ascl:1409.004 (2014).

2. Planck Collaboration, Aghanim, N. *et al.* Planck 2018 results. VI. Cosmological parameters. *Astro. Astrophys.* **641**, A6 (2020).

3. Chisholm, J., Prochaska, J. X., Schaerer, D., Gazagnes, S. & Henry, A. Optically thin spatially resolved Mg II emission maps the escape of ionizing photons. *Mon. Not. Royal Astron. Soc.* **498**, 2554–2574 (2020).

4. Green, A. W. *et al.* DYNAMO - I. A sample of Hα-luminous galaxies with resolved kinematics. *Mon. Not. Royal Astron. Soc.* **437**, 1070–1095 (2014).

5. Norris, R. P., Crawford, E. & Macgregor, P. Odd Radio Circles and Their Environment. *Galaxies* **9**, 83 (2021).

6. Johnson, B. D., Leja, J., Conroy, C. & Speagle, J. S. Stellar Population Inference with Prospector. *Astrophys. J. Suppl.* **254**, 22 (2021).

7. Conroy, C., Gunn, J. E. & White, M. The Propagation of Uncertainties in Stellar Population Synthesis Modeling. I. The Relevance of Uncertain Aspects of Stellar Evolution and the Initial Mass Function to the Derived Physical Properties of Galaxies. *Astrophys. J.* **699**, 486 (2009).

8. Aihara, H. *et al.* The Eighth Data Release of the Sloan Digital Sky Survey: First Data from SDSS-III. *Astrophys. J. Suppl.* **193**, 29 (2011).

9. Wright, E. L. *et al.* The Wide-field Infrared Survey Explorer (WISE): Mission Description and Initial On-orbit Performance. *Astron. J.* **140**, 1868–1881 (2010).

10. Kroupa, P. On the variation of the initial mass function. *Mon. Not. Royal Astron. Soc.* **322**, 231 (2001).

11. Ma, X. *et al.* The origin and evolution of the galaxy mass-metallicity relation. *Mon. Not. Royal Astron. Soc.* **456**, 2140 (2016).

12. Cheung, E. *et al.* Suppressing star formation in quiescent galaxies with supermassive black hole winds. *Nature* **533**, 504 (2016).

13. Roy, N. *et al.* Evidence of Wind Signatures in the Gas Velocity Profiles of Red Geysers. *Astrophys. J.* **913**, 33 (2021).

14. Roy, N. *et al.* Detecting Radio AGN Signatures in Red Geysers. *Astrophys. J.* **869**, 117 (2018).

15. Blandford, R., Meier, D. & Readhead, A. Relativistic Jets from Active Galactic Nuclei. *Ann. Rev. of Astron. Astrophys.* **57**, 467–509 (2019).

16. McDonald, M., Veilleux, S., Rupke, D. S. N. & Mushotzky, R. On the Origin of the Extended Hα Filaments in Cooling Flow Clusters. *Astrophys. J.* **721**, 1262–1283 (2010).

17. Girelli, G. *et al.* The stellar-to-halo mass relation over the past 12 Gyr. I. Standard ΛCDM model. *Astro. Astrophys.* **634**, A135 (2020).

18. Best, P. N. & Heckman, T. M. On the fundamental dichotomy in the local radio-AGN population: accretion, evolution and host galaxy properties. *Mon. Not. Royal Astron. Soc.* **421**, 1569 (2012).

Author Contributions   D.S.N.R. and A.L.C. conceived the observations, following C.A.T.'s suggestion that ORCs may be similar to the galaxies we have been studying. A.L.C. obtained the observing time, S.P. performed the KCWI observations and led the data reduction. A.L.C. performed all of the data analysis, with input from D.S.N.R. C.L. ran the starburst-wind model simulation, and K.W. performed the SED fitting.

A.L.C. wrote the manuscript, with input from all coauthors. Figures were created by S.P., A.L.C., K.W., C.L., and R.H.
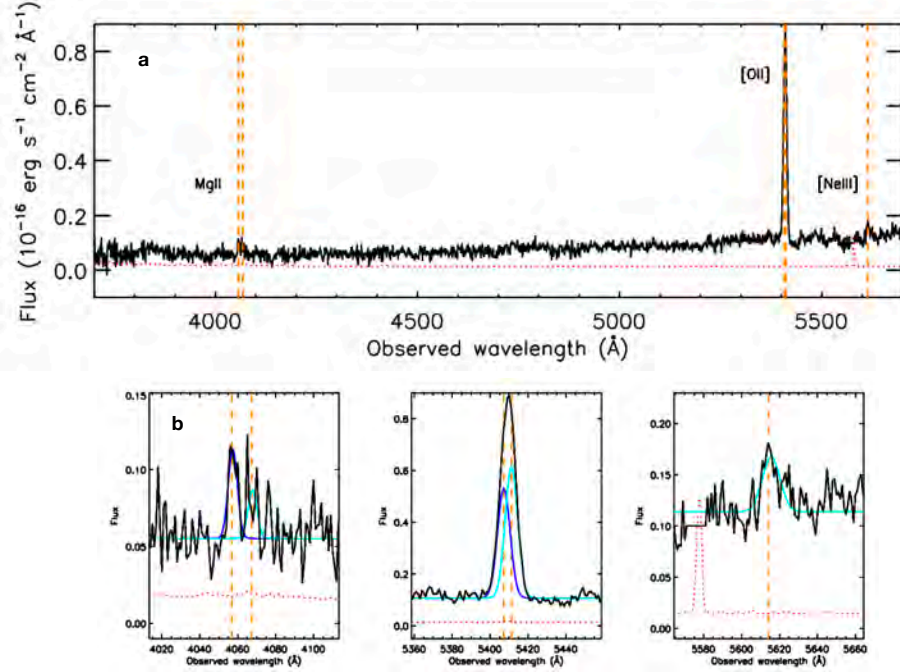
Extended Data Fig. 1 **Spatially-integrated spectrum of the gas nebula and host galaxy stellar continuum emission in ORC4.** (a) Strong [O II] 3726, 3729 Å and weak Mg II 2796, 2803 Å and [Ne III] 3869 Å emission are observed in a spatially-integrated spectrum of ORC4 (spanning the inner 26x26 kpc), at wavelengths that correspond to $z = 0.4512$; weak stellar continuum is also detected. The solid black line shows the observed spectrum, the pink dotted line is the 1σ error spectrum, and the orange dashed vertical lines indicate the observed wavelengths of Mg II, [O II], and [Ne III] at the spectroscopic redshift of the source. (b) Gaussian fits to the Mg II and [O II] emission doublets and the [Ne III] singlet in the spatially-integrated spectrum. Blue and cyan lines show fits to the individual emission lines in each doublet.
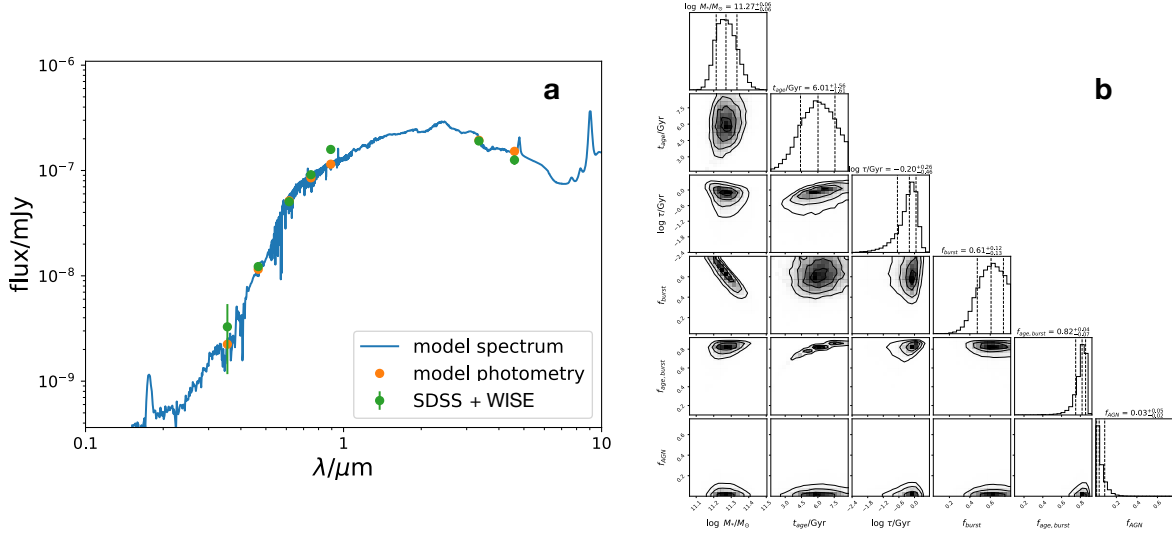
Extended Data Fig. 2 **Spectral energy distribution (SED) fit to optical SDSS and near infrared WISE photometry of ORC4.** (a) The observed photometry of ORC4 is shown as green circles with 1 σ error bars, while orange circles show the photometry implied from the best fit stellar population model, including an AGN contribution, which is shown in blue. Flux values are given in mJy and observed frame wavelengths in μm. (b) The derived distributions from the SED fit for the stellar mass, stellar age, star formation history parameters, and AGN contribution for ORC4, as well as the covariance between the parameters.
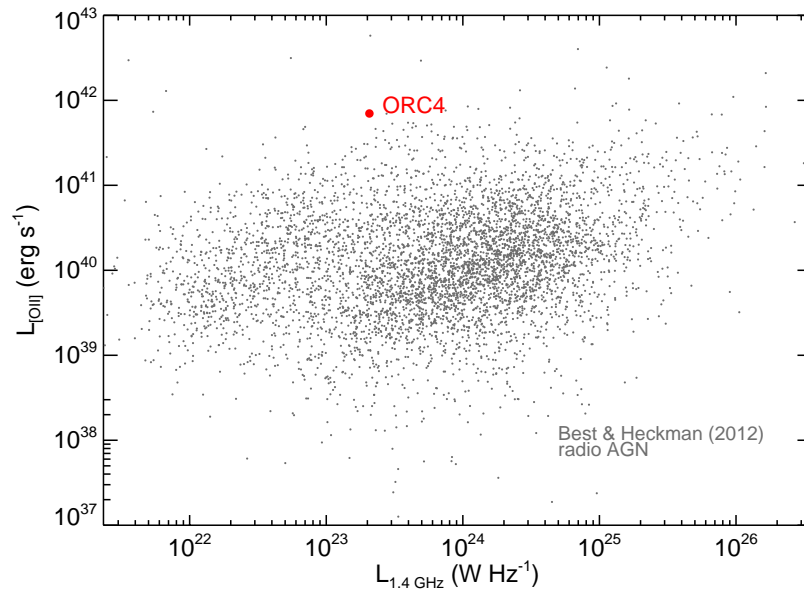
Extended Data Fig. 3 **Comparison of ORC4 radio continuum and [O II] line luminosity to radio AGN.** The 1.4 GHz radio continuum luminosity and [O II] emission line luminosity of ORC4, shown with a red circle, compared to the radio-loud AGN sample of Best & Heckman (2012)[18], shown with grey points. The [O II] luminosity of ORC4 is two orders of magnitude higher than the median value for an AGN with the same 1.4 GHz radio continuum luminosity.